Estimation of spectral solar irradiance in the ecliptic plane using synthetic solar surface magnetograms

I. de Oliveira[1], K. Sowmya[1], N.-E. Nèmec[2], and A. I. Shapiro[1]

[1]Max Planck Institute for Solar System Research, Justus-von-Liebig-Weg 3, 37077 Göttingen, Germany
[2]Institute for Astrophysics and Geophysics, Georg-August-Universität Göttingen, Friedrich-Hund-Platz 1, 37077 Göttingen, Germany

Key Points:

- We estimate the solar irradiance at any point in the ecliptic plane, accounting for the evolution of magnetic features on the solar surface.
- The method agrees for values in the ultraviolet but disagrees for the TSI when compared to the interpolation of Earth-based measurements.
- We calculate the correlation between our method and the phase shifting and the interpolation of Earth-based measurements of irradiance.

Corresponding author: I. de Oliveira, `oliveira@mps.mpg.de`

Abstract

The primary external energy input to planetary atmospheres comes from solar radiation. Accurate estimates of solar irradiance are needed in order to understand atmospheric conditions at other planets. Many studies have interpolated Earth-based irradiance measurements at other planets, disregarding the evolution of solar features, which are responsible for the irradiance variability. We present an approach for assessing solar irradiance at other planets by using synthetic full surface magnetograms of the Sun, generated by the Surface Flux Transport Model, and then converted into sunspots and faculae areas. Following the Spectral And Total Irradiance REconstruction approach, we compute the irradiance as the sum of contributions from sunspots, faculae, and the quiet Sun. We calculate the S-index, which is a proxy for near-ultraviolet irradiance, and the total solar irradiance, which is the wavelength-integrated value. We demonstrate that a simple phase shift of the Earth-observed total solar irradiance does not produce reliable estimates in the ecliptic. By comparing and correlating our results with the interpolated measurements, we find that the two models agree in the S-index variability, because faculae have a long lifetime, so the effect of the solar rotation becomes less important. Conversely, the methods disagree strongly in the total solar irradiance, since sunspots have a short lifetime, and the interpolation does not take into account their emergence and evolution on the far-side of the Sun, as it only uses the information of the disc visible for an Earth-bound observer.

1 Introduction

Solar radiation is the main source of external energy input to planetary atmospheres, playing a crucial role in the atmospheric structure and composition. In particular, the ultraviolet (UV) irradiance drives the photochemistry of the Earth's middle atmosphere (Gray et al., 2010), while the extreme ultraviolet (EUV) radiation is responsible for the photochemistry of the upper atmospheres of the planets in the Solar System (Fox et al., 2008). A number of general circulation models have been employed in order to understand the mechanisms that rule the atmospheric behavior. These models need, as an input, the values of solar irradiance entering the planetary atmosphere. However, the direct measurements of such irradiance are scarce, so that it must be obtained with modelling.

Several studies have used measurements made at Earth to evaluate the solar irradiance at other planets (e.g. Ramstad et al., 2015; Peter et al., 2014). These studies are based on the assumption that irradiance from the non-rotating Sun is constant and, thus, the only source of irradiance variability is the solar rotation (hereafter referred as the lighthouse approximation). Then, to obtain the irradiance entering the atmosphere of a planet, the measurements made from Earth are either phase-shifted (see Section 3.1) or interpolated (see Section 3.2) according to the relative position of the Earth and the planet and then scaled to the Sun-planet distance (Thiemann et al., 2017, 2021).

There have been efforts to test the accuracy of the lighthouse approximation in the literature. For example, Thiemann et al. (2021) used measurements from the Extreme Ultraviolet Monitor (EUVM, Eparvier et al., 2015) onboard the Mars Atmosphere and Volatile EvolutioN (MAVEN) spacecraft to conclude that the error introduced by the lighthouse approximation can be comparable to the amplitude of the solar rotational variability. Quémerais et al. (2019) developed an algorithm which combines measurements from the Solar Wind ANisotropies (SWAN) Solar Heliospheric Observatory (SOHO) Lyman-α photometer with Earth-based solar flux measurements to derive the irradiance at Lyman-α for any direction in the ecliptic plane. They found that the SWAN-based method is superior to the interpolation at periods of high solar activity. On the contrary, the interpolation method works better than the SWAN-based method at periods of low solar activity.

The lighthouse approximation introduces an error that depends on the angle within the ecliptic plane between Earth and the planet of interest, centered on the Sun. This Earth-Sun-planet angle (ϕ) is shown in Figure 1. This error is a consequence of the constantly evolving distribution of magnetic fields on the solar surface. The magnetic fields emerge from the interior of the Sun, forming active regions on the surface, which evolve and decay on timescales from days to months (see e.g. Solanki et al., 2013, and references therein). In the absence of active regions, the solar irradiance is constant. In this case, the solar irradiance measured at Earth can be scaled to other positions in the Solar System with a simple function of distance. The active regions, however, make the solar surface heterogeneous and lead to anisotropic solar irradiance, as well as the temporal variability of the irradiance.

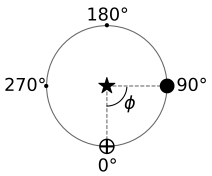

Figure 1. Earth-Sun-planet angle (ϕ), within the ecliptic plane. The Earth and the planet of interest are depicted by the symbols $\oplus$ and the full circle, respectively, and the star depicts the Sun. Solar rotation is anti-clockwise.

There are two main sources of solar variability on the timescales from days to months. The first is brought about by solar rotation: the active regions rotate in and out of view, similar to the behavior of a lighthouse. The second is attributed to the evolution of active regions. Nèmec et al. (2020) showed that the variability of the solar irradiance in the visible spectral domain is dominated by rotation for timescales between 4-5 days and the synodic solar rotation period (27.3 days). For timescales shorter than 4-5 days or longer than a solar rotation, the variability is dominated by the evolution and emergence pattern of magnetic features, which is not taken into consideration by the lighthouse approximation.

In this study, we present a method for estimating solar irradiance at different positions within the ecliptic plane of the Solar System, for the total solar irradiance (TSI, i.e. spectrally-integrated irradiance) and for the S-index (a proxy for near-ultraviolet). We take into consideration the evolution of active regions in the Sun and follow an approach rooted in the Spectral And Total Irradiance REconstruction model (SATIRE, Fligge et al., 2000; Krivova et al., 2003, 2011). Our SATIRE-inspired approach is described in Section 2 and then compared to both simple shifting of irradiance measurements and the interpolation method in Section 3. The conclusions of this work are drawn in Section 4.

2 Methods

In order to calculate the TSI and the S-index, we combine spectra of the quiet Sun (i.e. regions on the solar surface free from any visible manifestations of magnetic activity) and the magnetic features with their corresponding area coverages on the visible solar disc. Each of these aspects will be covered in this section.

2.1 Spectral and total solar irradiance

The SATIRE-inspired approach makes use of the intensity of the quiet Sun and of magnetic features, weighted by their areas on the solar disc. It takes into account the distribution and time evolution of magnetic features on the full solar surface so that the

irradiance variability in any given direction can be directly calculated. The approach is based on the assumption that solar irradiance variations on timescales longer than one day can be explained by variations in the surface magnetic fields (Fligge et al., 2000; Krivova et al., 2003).

In this approach, the spectral solar irradiance (SSI) at the Earth-Sun-planet angle ϕ (see Figure 1), at an orbital inclination θ, for a certain time t and wavelength λ is computed as the sum of two components:

$$E^{\phi\theta}(t,\lambda) = E_{\rm q}(\lambda) + E_{\rm a}^{\phi\theta}(t,\lambda). \tag{1}$$

Then, the TSI is obtained by integrating the SSI calculated using Eq. 1 over all wavelengths.

In Eq. 1, $E_{\rm q}(\lambda)$ is the time-independent spectral irradiance from the quiet Sun. $E_{\rm q}(\lambda)$ does not depend on ϕ and θ, and is given by

$$E_{\rm q}(\lambda) = \sum_i I_{\rm q}(\lambda,\mu_i)\Delta\Omega_i, \tag{2}$$

where $I_{\rm q}(\lambda,\mu_i)$ is the intensity emerging from the quiet Sun for a given λ at a disc position given by μ_i , where μ is the cosine of the heliocentric angle. The solar surface is divided into many pixels indexed with i (see Section 2.2) and $\Delta\Omega_i$ is the solid angle subtended by the i-th pixel as seen from the planet.

The term $E_{\rm a}^{\phi\theta}(t,\lambda)$ in Eq. 1 represents the contribution to the SSI from magnetic activity, and can be decomposed as

$$\begin{aligned} E_{\rm a}^{\phi\theta}(t,\lambda) = &\sum_i \alpha_{\rm u}^{i\phi\theta}(t)[I_{\rm u}(\lambda,\mu_i) - I_{\rm q}(\lambda,\mu_i)]\Delta\Omega_i \\ &+ \sum_i \alpha_{\rm p}^{i\phi\theta}(t)[I_{\rm p}(\lambda,\mu_i) - I_{\rm q}(\lambda,\mu_i)]\Delta\Omega_i \\ &+ \sum_i \alpha_{\rm f}^{i\phi\theta}(t)[I_{\rm f}(\lambda,\mu_i) - I_{\rm q}(\lambda,\mu_i)]\Delta\Omega_i. \end{aligned} \tag{3}$$

Here, $I(\lambda,\mu_i)$ are the intensities of the magnetic features, namely, sunspot umbrae (u), sunspot penumbrae (p), and faculae (f). Unruh et al. (1999) have shown that including only the quiet Sun, sunspots, and faculae in the computations is adequate to explain the observed SSI and TSI variations (see e.g. Solanki et al., 2013; Ermolli et al., 2013). We employ the intensities computed by Unruh et al. (1999) with the use of the ATLAS9 radiative transfer code (Kurucz, 1992; Castelli & Kurucz, 1994), under the assumption of local thermodynamic equilibrium (LTE).

The intensities are derived for 1221 wavelengths, ranging from 9.09 nm to 10020 nm, with varying spectral resolution, but only values computed above 160 nm can be trusted, due to the assumption of LTE in ATLAS9 (Tagirov et al., 2019). To account for the centre-to-limb variation of the intensity, the intensities are calculated for 11 positions on the solar disc corresponding to $\mu = 1.0$ (disc center), 0.9, 0.8, 0.7, 0.6, 0.5, 0.4, 0.3, 0.2, 0.1, and 0.05. For intermediate disc positions, i.e. when μ_i of the pixel is different from these 11 values, the intensities are interpolated to the value of μ_i.

In Eq. 3, $\alpha^{i\phi\theta}(t)$ are the fractional area coverages per pixel by a given magnetic feature. Depending on ϕ and θ, an observer sees different parts of the solar surface, i.e., the visible solar disc changes. The dependence of the SSI on the observer's location comes solely from $E_{\rm a}^{\phi\theta}(t,\lambda)$, because the disc area coverages of sunspots and faculae depend on ϕ and θ. Therefore, the calculation of the SSI for different ϕ and θ angles requires that the distribution of sunspots and faculae over the entire solar surface is known, in addition to their intensities.

In the following section, we describe the method used to obtain the area coverages of magnetic features that are needed to compute the SSI and TSI at various locations of the observer. Several studies have used this method to model solar irradiance at arbitrary inclinations (see e.g. Nèmec et al., 2020; Sowmya, Shapiro, et al., 2021). We note that for any ϕ and θ, an observer sees only half of the solar surface and therefore the summations in Eqs. 2 and 3 are carried out only over the pixels on the visible disc. Furthermore, to compare our results with those which use measurements made exclusively on Earth, we limit our analysis to the solar disc as observed from the ecliptic plane, and therefore the superscript θ will be omitted from now on.

2.2 Area coverages

We use the spots and faculae area coverage maps obtained by Nèmec et al. (2020), who utilised the Surface Flux Transport Model (SFTM) in the form presented in Cameron et al. (2010). We summarise their approach here briefly, but refer to Nèmec et al. (2020) for details.

In the SFTM, magnetic flux emerges as bipolar magnetic regions and, once emerged, the flux evolves due to advection, diffusion and large scale flows (i.e. the meridional flow and differential rotation). The emergence of the bipolar magnetic regions is based on the semi-empirical input record of sunspot groups, as described in Jiang et al. (2011), with the addition that the emergence longitude of the bipolar magnetic regions is randomised in order to get the full surface distribution of the regions, as needed for our purpose. We note that the statistical input record preserves the latitudes of emergence (i.e. the solar butterfly diagram), but due to the nature of the semi-empirical record, the actual sizes and emergence of the active regions cannot be directly compared on a day-to-day basis to the observed distribution on the Sun. While the record by Jiang et al. (2011) dates back to 1700, we only utilise the synthesized solar cycle 22, which represents a cycle of intermediate activity level.

Subsequently, the flux distribution is converted into spot and faculae areas. Following the input record, sunspots are immediately emerged at their largest size, i.e. we neglect the growing phase. On the day of emergence, Nèmec et al. (2020) calculated the size of the spots using the given areas in the input record, but needed to add a simple model to take into account the growth and decay of the spots. Penumbral area coverages are taken as 80% of the spot areas, while the remaining 20% is attributed to umbrae. Using the spatial and temporal distribution of spots, the magnetic flux in each pixel of the full surface map is corrected for the spot flux. The remaining magnetic field in the pixel is ascribed to faculae. The area coverages of faculae are determined following the saturation threshold approach of the SATIRE model (Fligge et al., 2000; Krivova et al., 2003). From the full surface maps of area coverages, the coverages on the visible disc for any ϕ can be computed by making appropriate geometrical transformations (see e.g. Sowmya, Nèmec, et al., 2021).

Figure 2 illustrates an example of the synthetic distribution of magnetic features on the full solar surface and the visible discs corresponding to ϕ angles of 0°, 90°, 180°, and 270°. The spatial distribution as well as the area coverages of spots and faculae on the visible disc are very different depending on ϕ, as clearly shown by the orthographic projections in Figure 2.

2.3 S-index

The Mg II spectral lines around 280 nm exhibit one of the largest solar irradiance variability in the near-UV. Due to this, the Mg II index (core to wing ratio) is used as a proxy for the irradiance variability in the UV and EUV regime. The Mg II index is also shown to be a better proxy for solar EUV than the widely used F10.7 index (Viereck

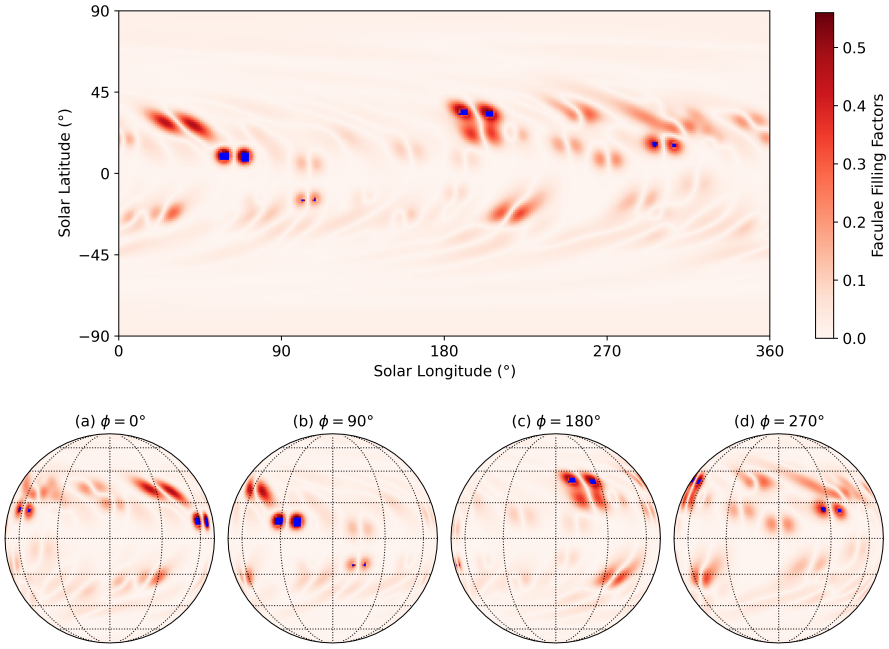

Figure 2. Snapshot of a synthetic distribution of faculae (red shades) and sunspots (blue pixels). Top: full surface map. Bottom: orthographic projections centered at the ϕ angle indicated above each panel. An observer placed at $\phi = 0°$ views the visible solar disc as in panel (a), for example.

et al., 2001). Very accurate and high resolution spectra of the Mg II lines synthesized in non-LTE as a function of μ are needed to correctly determine the Mg II index and its dependence on ϕ. Since such detailed modelling is currently unavailable and beyond the scope of this work, we instead use the Ca II H and K lines to investigate the irradiance changes in the near-UV. Such a choice is directly driven by the strong linear correlation between the irradiance in the Mg II and Ca II lines (DeLand & Marchenko, 2013).

We quantify the variability in Ca II via the well-known chromospheric activity indicator, namely the S-index (Vaughan et al., 1978). The S-index is calculated as the ratio of the summed fluxes in the Ca II H and K line cores to the summed fluxes in two spectral regions near the blue wing of the K line and the red wing of the H line. This index was established by the Mt. Wilson Observatory, and has been recorded for lower main-sequence stars since 1966 (Wilson, 1978).

The formation of Ca II H and K lines spans a wide range of heights in the solar atmosphere. The line cores are formed in the chromosphere, above the solar photosphere, where LTE assumptions are no longer valid. Sowmya, Shapiro, et al. (2021) followed a non-LTE approach to compute the emergent intensities of the quiet Sun and faculae, using the RH code (Uitenbroek, 2001). Here, again, the intensities are computed for different disc position, as explained in Section 2.1, in order to account for center-to-limb variations.

We use the spectra from Sowmya, Shapiro, et al. (2021) in Eqs. 2 and 3 to determine the near-UV SSI variability, neglecting the contribution from spots, since the variability in the Ca II H and K lines are mainly driven by faculae, as shown by Sowmya, Shapiro, et al. (2021) and Sowmya et al. (2023). The S-index is then obtained according to Eq. 1 of Sowmya, Shapiro, et al. (2021).

3 Results and discussion

The synthetic calculations of TSI and S-index in this work are performed for two one-year periods within solar cycle 22, using the methods presented in Sections 2.1 and 2.3. The first year is a period of high solar activity and it is centered on the day with the maximum disc area coverage of faculae during the cycle. The second is a period of low solar activity and comprises the last 365 days of solar cycle 22. Figure 3 shows the obtained TSI for the whole solar cycle 22, as well as the chosen periods of high and low solar activity.

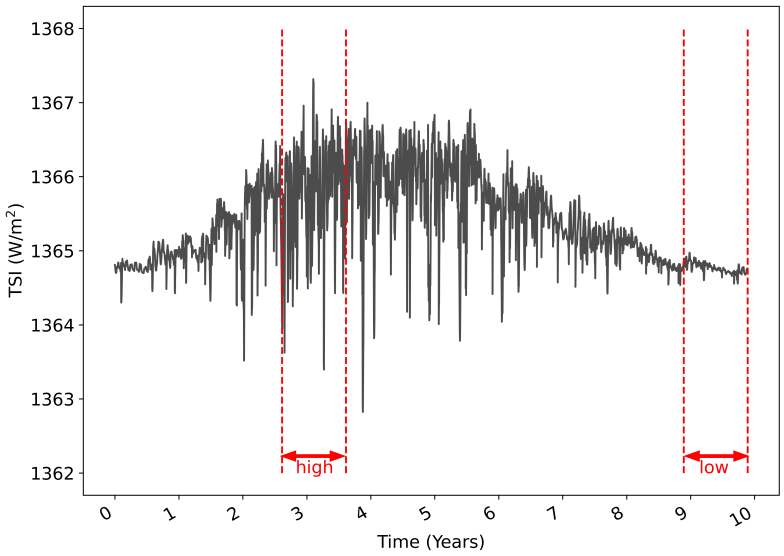

Figure 3. Synthetic TSI based on the magnetic flux of the visible disc for solar cycle 22. The one-year time periods of high and low solar activity used in this work are marked by red dashed lines.

We define the normalized variability on the time scale of a solar rotation as

$$\Delta E^{\phi}(t,\lambda) = \frac{E^{\phi}(t,\lambda) - \langle E^{\phi}(t,\lambda)\rangle_{81}}{\langle E^{\phi}(t,\lambda)\rangle_{81}}, \tag{4}$$

where $\langle E^{\phi}(t,\lambda)\rangle_{81}$ is the moving average with an 81-days time window centered on t. We use a time window of 81-days, which is the equivalent to three solar rotations, in order to remove the effects that arise due to the transit of the magnetic features.

For the S-index, we simply calculate the rotational variability as

$$\Delta S^{\phi}(t) = S^{\phi}(t) - \langle S^{\phi}(t)\rangle_{81}, \tag{5}$$

where $S^{\phi}(t)$ is the S-index at time t and angle ϕ, and $\langle S^{\phi}(t)\rangle_{81}$ is the 81-days moving average.

3.1 Phase shifts and cross-correlation analysis

In the phase shift approach, the irradiance at the planet of interest is obtained by simply phase shifting the irradiance measurements made at Earth and scaling them to the Sun-planet distance. In this approach, we neglect the evolution of active regions and assume that in the absence of solar rotation, the solar irradiance is constant.

Here, we perform an experiment to assess the accuracy of the phase shift approach at three different ϕ angles in the plane of the solar equator: $90°, 180°$, and $270°$ (see Figure 1). According to the phase shift approach, the irradiance values at these angles are

$$E^{90^\circ}(t,\lambda) = E^{0^\circ}(t - 7\ d, \lambda) \tag{6}$$

$$E^{180^\circ}(t,\lambda) = E^{0^\circ}(t - 14\ d, \lambda) \tag{7}$$

$$E^{270^\circ}(t,\lambda) = E^{0^\circ}(t - 21\ d, \lambda), \tag{8}$$

with t in days (d). The time periods are equivalent to the angular distance, assuming the synodic solar rotation to be $\sim$ 28 days. The irradiance at $\phi = 90°$ is expected to be the irradiance at $\phi = 0°$ a quarter of a solar rotation (seven days) earlier, and so on for the other ϕ angles.

Figure 4 shows the comparison between TSI values calculated with the phase shift approach (i.e. with Eqs. 6–8, see blue, green, and red curves) and with the SATIRE-based approach (i.e. with Eqs. 1–3, see black curves). The comparison is given for periods of high (left panels) and low (right panels) solar activity during solar cycle 22. We note that the dips in the time series are indicative of spot transits. Since the spots are dark, they reduce the TSI. On the contrary, the peaks are caused by faculae, which are bright regions that increase the TSI.

The variability of the S-index computed with the phase shift and with SATIRE-based approaches is shown in Figure 5, following the same color scheme as in Figure 4. We note that the S-index calculations are performed by neglecting spots, since Sowmya et al. (2023) showed that the solar S-index and its variability are mainly driven by faculae. Hence, the variability seen in Figure 5 are attributed to faculae. The solar rotational cycles are clearly visible in the time series at both high and low activity periods.

In Table 1, we show the linear Pearson correlation coefficients obtained for each of the cases presented in Figures 4 and 5. The correlation between the reference and the shifted TSI time series is poor during both periods of solar activity. In addition, the correlation worsens with increasing ϕ. This can be attributed to spots which dominate TSI at shorter timescales. The spots are short-lived and evolve quickly on the solar surface. Because of that, the visible disc at various ϕ differs considerably and the correlation becomes low when a shift of the order of a few days is applied. This suggests that a simple phase shift of the irradiance time series is not a good solution for determining the TSI and its variability at different positions within the Solar System ecliptic plane.

The S-index curves at $\phi = 0°$ and at $\phi = 90°$ shifted by seven days (blue curves) show a very good correlation, with linear correlation coefficients above 0.9. The difference between these two time series at $\phi = 90°$ and the series at $\phi = 0°$ arises from the evolution of faculae over the course of seven days. Since the faculae survive on the solar surface longer than most spots, the time series recorded seven days apart still sees most of the original faculae features and thus the correlation between the time series is high. With increasing ϕ, the correlation between the time series generally decreases, although the correspondence is still reasonably high. This indicates that shifting the so-

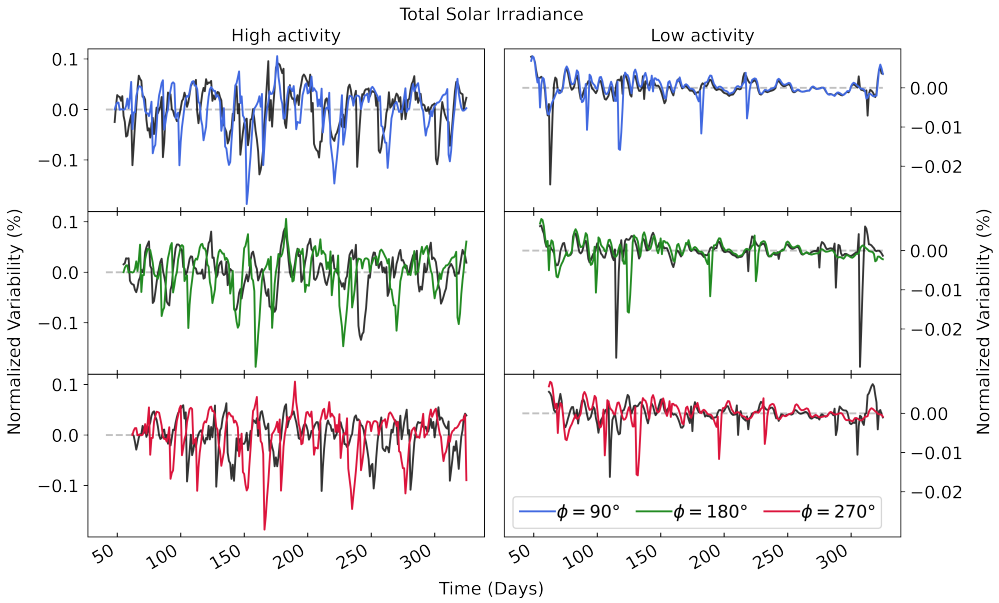

Figure 4. Synthetic time series of the normalized TSI variability for periods of high (left) and low (right) solar activity. The panels show the calculated (black) and phase shifted (colors) variability. From top to bottom, the panels show $\phi = 90°$ (blue), $\phi = 180°$ (green), and $\phi = 270°$ (red).

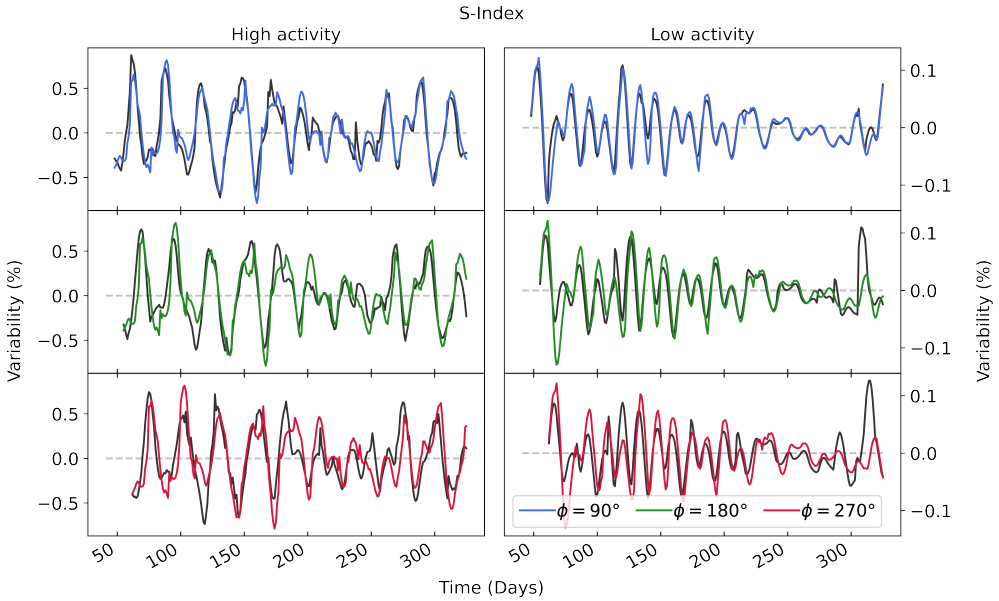

Figure 5. The same as in Figure 4, but for the S-index variability.

lar irradiance time series measured at Earth to other positions within the ecliptic plane works relatively better for S-index than for TSI.

We also determine the cross-correlation between the time series. With this analysis, our aim is to find how many days (forward or backward) the irradiance time series at $\phi = 90°, 180°$, and $270°$ should be shifted in order to achieve the highest correlation

Table 1. *Correlation Coefficients Between the Calculated and the Phase Shifted Time Series of Irradiance.*

	High activity		Low activity	
ϕ	TSI	S-index	TSI	S-index
90°	0.39	0.92	0.47	0.93
180°	0.10	0.84	0.17	0.75
270°	−0.10	0.75	0.18	0.63

Table 2. *Results of the Cross-Correlation Analysis Between the Time Series.*

	High activity				Low activity			
	TSI		S-index		TSI		S-index	
ϕ	Shift (days)	r	Shift (days)	r	Shift (days)	r	Shift (days)	r
90°	−6	0.45	−6	0.92	−7	0.47	−6	0.94
180°	−22	0.19	−13	0.87	−5	0.30	+13	0.82
270°	+4	0.38	+7	0.90	+7	0.41	+7	0.88

Note. Given are the maximum correlation coefficients (r) and their corresponding shifts with respect to the time series at $\phi = 0°$. Negative shifts indicate preceding days, while positive shifts indicate following days.

coefficient, r, to the time series at $\phi = 0°$. This is done by shifting the time series day by day, with a time window ranging from a solar rotation in the past to a solar rotation in the future, and comparing them with the time series at $\phi = 0°$. Table 2 shows the results of the cross-correlation analysis. Negative shifts indicate preceding days (the same logic as in Eqs. 6–8), while positive shifts indicate following days.

As discussed previously, an angular distance of $\phi = 90°$ should correspond approximately to −7 days, $\phi = 180°$ to −14 days, and $\phi = 270°$ to −21 days. The cross-correlation analysis gives the expected result for $\phi = 90°$, even though the coefficients are relatively low for the TSI. For higher ϕ angles, the maximum correlation coefficients for the TSI do not seem to have any physical meaning, since the shifts are very distant from what is expected. As for the S-index, some of the maximum coefficients are achieved when the time series are shifted one entire solar rotation ahead of what is expected (positive shifts). From Figures 4 and 5 and Tables 1 and 2, we infer that a simple phase shift is not sufficient to provide good correlation results and, accordingly, irradiance estimates.

3.2 Comparison with interpolated Earth-based measurements

As described by Thiemann et al. (2017), the interpolation method estimates the irradiance at a certain planet (or angle ϕ within the ecliptic plane) for a day t_d, by using measurements at Earth ($E_\oplus$) made before ($t_d - \Delta t_1$) and after ($t_d + \Delta t_2$) the visible solar disc rotates past the planet. The time differences Δt_1 and Δt_2 follow the same logic as in Eqs. 6 to 8. For example, if the Earth-Sun-planet angle ϕ is 90° today, the irradiance at the planet would be estimated as the weighted sum of the irradiance at Earth ∼7 days ago and ∼21 days in the future. The interpolation is given by

$$E(t_d, \phi) = \frac{w_1\ E_\oplus(t_d - \Delta t_1) + w_2\ E_\oplus(t_d + \Delta t_2)}{r^2(t_d)}, \tag{9}$$

where $r^2(t_d)$ is the distance between Earth and the planet on day t_d, in AU. The measurements are linearly interpolated and weighted, and the weights w_1 and w_2 are pro-

Table 3. *Correlation Coefficients Between the Calculated and the Interpolated Time Series of Irradiance.*

	High activity		Low activity	
ϕ	TSI	S-index	TSI	S-index
90°	0.30	0.93	0.49	0.93
180°	0.17	0.93	0.21	0.87
270°	0.24	0.93	0.45	0.90

portional to the periods Δt_1 and Δt_2. In the example given, the weights Δt_1 and Δt_2 would be 0.75 and 0.25, respectively. For a more detailed explanation of the method, see Section 2.1 from Thiemann et al. (2017).

We apply the interpolation method to the irradiance time series at $\phi = 0°$, and determine the irradiance at $\phi = 90°, 180°$, and 270°. Then, we compare these interpolated time series to the ones evaluated at $\phi = 90°, 180°$, and 270° using our SATIRE-inspired approach, by considering the Pearson correlation coefficient of the time series at each ϕ. The coefficients are shown in Table 3. Figure 6 shows such a comparison for the TSI during periods of high and low activity. The time series calculated using our SATIRE-inspired approach at ϕ (black curves) and the values interpolated from $\phi = 0°$ to $\phi = 90°, 180°$, and 270° (in colors) differ greatly.

The interpolation method misses the exact timing of most spot transits (valleys), especially for periods of high solar activity. During periods of low solar activity, extrapolating the data seems to overestimate the duration and/or intensity of the sunspots. For all three positions around the Sun, the correlation between the calculated and the interpolated TSI variability does not surpass 0.49. This suggests further that the interpolation of the TSI variability observed at Earth to other planets does not represent the true variability seen at those planets. By comparing Figures 4 and 6, however, the valleys and peaks characteristics of each time series are better reconstructed with the interpolation than with the phase shifting method.

Following the same scheme, Figure 7 shows the time series of the S-index variability at high and low activity periods. Contrary to the TSI case, the correlations between the calculated and interpolated S-index variability are high, and the curves look very similar. Again, the shapes of the interpolated irradiance time series are more in agreement to the ones obtained with the SATIRE-inspired approach than the ones estimated with the phase shifting method (Figure 5).

On one hand, the interpolation method works very well for the proxy of UV wavelengths because facular regions evolve very slowly, so that the evolution variability they induce is not significant on solar rotation timescales. On the other hand, the application of the interpolation method for the TSI or wavelengths which are dominated by sunspots would result in a very large error in the estimated irradiance.

4 Summary and conclusions

In this study, we present a method for estimating solar irradiance within the ecliptic plane. First, we use a synthetic statistical model of magnetic field transport, as well as semi-empirical information on active regions sources in order to build a synthetic model of faculae and spots area coverages observed at any position within the ecliptic plane during solar cycle 22. Then, we compute synthetic values of spectral solar irradiance at several Earth-Sun-planet angles in the Solar System using a method that is built on the SATIRE model for solar irradiance variability reconstruction.

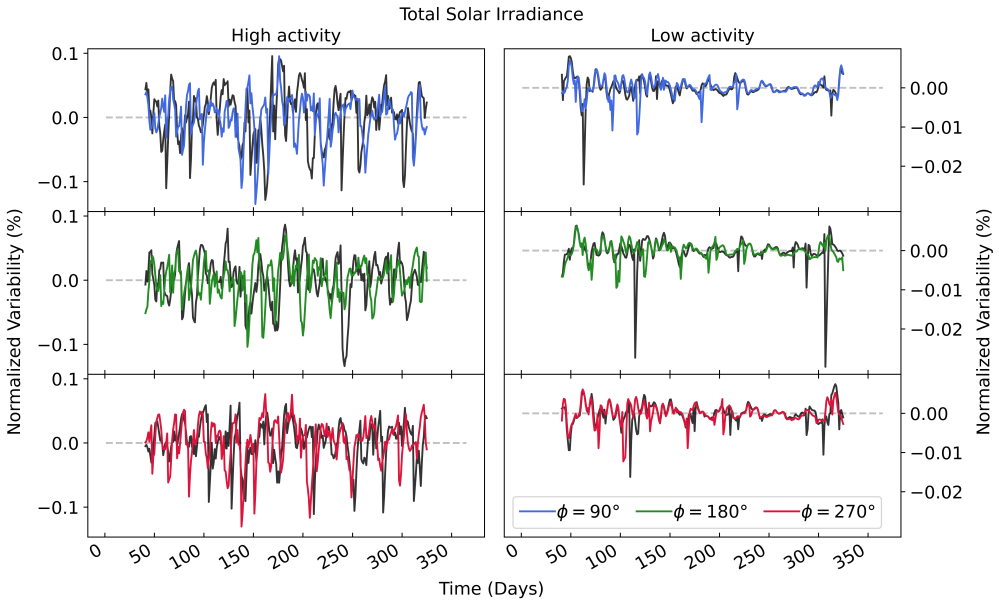

Figure 6. Synthetic time series of the normalized TSI variability for periods of high (left) and low (right) solar activity. The panels show the variability calculated using our SATIRE-inspired approach (black) and the interpolation method (colors). From top to bottom, the panels show $\phi = 90°$ (blue), $\phi = 180°$ (green), and $\phi = 270°$ (red).

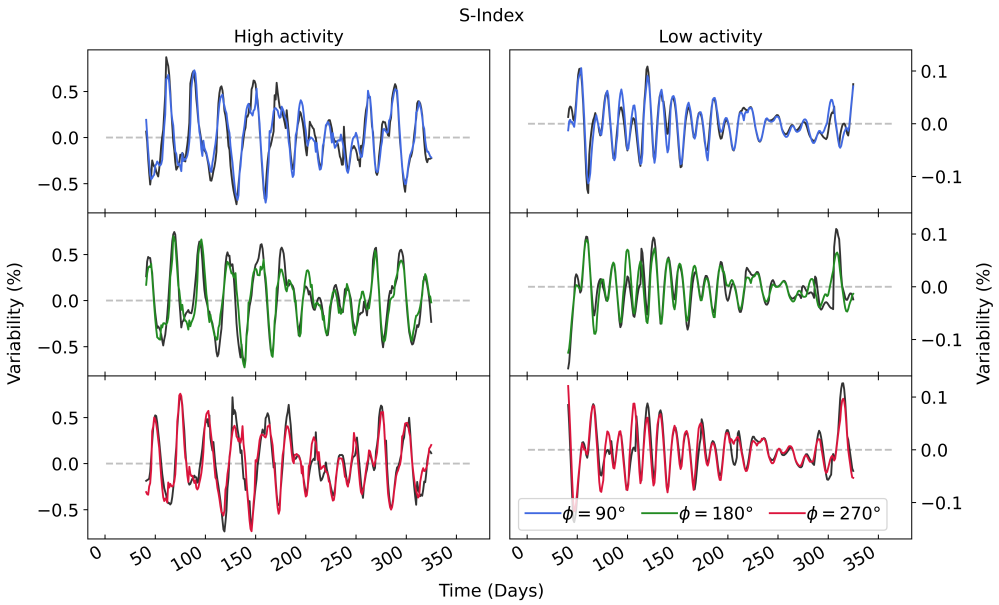

Figure 7. The same as in Figure 6, but for the S-index variability.

Using our SATIRE-inspired synthetic model, we evaluate the TSI and the S-index, which is a proxy for irradiance at near-UV wavelengths, at four Earth-Sun-planet angles: $\phi = 0°, 90°, 180°$, and $270°$, for a year of high solar activity and a year of low solar activity. We apply a simple phase shift to the time series at $\phi = 90°, 180°$, and $270°$, proportional to the solar rotation, and compare the results with the time series at $\phi =$

334 0°. We conclude that a simple phase shift of the data is not enough to obtain good es-
335 timates of solar irradiance.

336 We also compared our method with the traditional interpolation method (Thiemann
337 et al., 2017). This method consists of a "lighthouse" model, where Earth-based measure-
338 ments of SSI are interpolated to other planets assuming that irradiance variability is only
339 caused by solar rotation.

340 We investigate the correlation of the time series computed with our SATIRE-inspired
341 approach and the interpolated time series. The results show that there is a high corre-
342 lation between the interpolation and the SATIRE-inspired approach when it comes to
343 the S-index. Due to the relatively greater lifetime of faculae, which are the sources of
344 solar UV variability, the interpolation method is able to catch slow changes in irradiance.
345 However, the correlation drops significantly for the TSI, since it is dominated by sunspots,
346 which emerge, evolve, and decay very fast. In this case, the interpolation method can-
347 not properly account for the effect of spots, which are relatively short-lived and do not
348 survive a full solar rotation. The SATIRE-inspired approach directly calculates the TSI,
349 accounting for effects of faculae and spots, which is advantageous compared to the in-
350 terpolation method.

351 We point out that our SATIRE-inspired approach for evaluating irradiance is still
352 based on a synthetic model of full surface solar magnetograms and we used statistically
353 valid emergences of magnetic regions to calculate the irradiance, and not real data. There-
354 fore, the model is not capable of producing a nowcast estimation of solar irradiance. In
355 the future, we will use information of far-side helioseismology to derive the actual area
356 coverages of magnetic regions.

357 Open Research Section

358 The area coverages data and flux intensities used for the calculations of irradiance
359 in the study are available in De Oliveira (2024).

360 Acknowledgments

361 I. de O. would like to thank Laurent Gizon and Dan Yang for their contribution on re-
362 viewing the draft of this paper. This work was supported by the International Max Planck
363 Research School for Solar System Science at the University of Göttingen.

364 References

365 Cameron, R. H., Jiang, J., Schmitt, D., & Schüssler, M. (2010, August). Surface
366 Flux Transport Modeling for Solar Cycles 15-21: Effects of Cycle-Dependent
367 Tilt Angles of Sunspot Groups. *The Astrophysical Journal*, *719*(1), 264-270.
368 doi: 10.1088/0004-637X/719/1/264

369 Castelli, F., & Kurucz, R. L. (1994, January). Model atmospheres for Vega. *Astron-*
370 *omy & Astrophysics*, *281*, 817-832.

371 DeLand, M., & Marchenko, S. (2013, April). The solar chromospheric Ca and Mg in-
372 dices from Aura OMI. *Journal of Geophysical Research (Atmospheres)*, *118*(8),
373 3415-3423. doi: 10.1002/jgrd.50310

374 De Oliveira, I. (2024, February). *Data from: Estimation of solar irradiance*
375 *in the ecliptic plane using synthetic solar surface magnetograms.* Zen-
376 odo. Retrieved from `https://doi.org/10.5281/zenodo.10630214` doi:
377 10.5281/zenodo.10630214

378 Eparvier, F. G., Chamberlin, P. C., Woods, T. N., & Thiemann, E. M. B. (2015,
379 December). The Solar Extreme Ultraviolet Monitor for MAVEN. *Space Sci-*
380 *ence Reviews*, *195*(1-4), 293-301. doi: 10.1007/s11214-015-0195-2

Ermolli, I., Matthes, K., Dudok de Wit, T., Krivova, N. A., Tourpali, K., Weber, M., ... Woods, T. N. (2013). Recent variability of the solar spectral irradiance and its impact on climate modelling. *Atmospheric Chemistry & Physics*, *13*(8), 3945-3977. doi: 10.5194/acp-13-3945-201310.5194/acpd-12-24557-2012

Fligge, M., Solanki, S. K., & Unruh, Y. C. (2000, January). Modelling irradiance variations from the surface distribution of the solar magnetic field. *Astronomy & Astrophysics*, *353*, 380-388.

Fox, J. L., Galand, M. I., & Johnson, R. E. (2008, August). Energy Deposition in Planetary Atmospheres by Charged Particles and Solar Photons. *Space Science Reviews*, *139*(1-4), 3-62. doi: 10.1007/s11214-008-9403-7

Gray, L. J., Beer, J., Geller, M., Haigh, J. D., Lockwood, M., Matthes, K., ... White, W. (2010, October). Solar Influences on Climate. *Reviews of Geophysics*, *48*(4), RG4001. doi: 10.1029/2009RG000282

Jiang, J., Cameron, R. H., Schmitt, D., & Schüssler, M. (2011, April). The solar magnetic field since 1700. II. Physical reconstruction of total, polar and open flux. *Astronomy & Astrophysics*, *528*, A83. doi: 10.1051/0004-6361/201016168

Krivova, N. A., Solanki, S. K., Fligge, M., & Unruh, Y. C. (2003, February). Reconstruction of solar irradiance variations in cycle 23: Is solar surface magnetism the cause? *Astronomy & Astrophysics*, *399*, L1-L4. doi: 10.1051/0004-6361:20030029

Krivova, N. A., Solanki, S. K., & Unruh, Y. C. (2011, February). Towards a long-term record of solar total and spectral irradiance. *Journal of Atmospheric and Solar-Terrestrial Physics*, *73*(2-3), 223-234. doi: 10.1016/j.jastp.2009.11.013

Kurucz, R. L. (1992, March). Remaining Line Opacity Problems for the Solar Spectrum. *Revista Mexicana de Astronomia y Astrofisica*, *23*, 187.

Nèmec, N. E., Shapiro, A. I., Krivova, N. A., Solanki, S. K., Tagirov, R. V., Cameron, R. H., & Dreizler, S. (2020, April). Power spectra of solar brightness variations at various inclinations. *Astronomy & Astrophysics*, *636*, A43. doi: 10.1051/0004-6361/202037588

Peter, K., Pätzold, M., Molina-Cuberos, G., Witasse, O., González-Galindo, F., Withers, P., ... Tyler, G. L. (2014). The dayside ionospheres of Mars and Venus: Comparing a one-dimensional photochemical model with MaRS (Mars Express) and VeRa (Venus Express) observations. *Icarus*, *233*, 66-82. Retrieved from `https://www.sciencedirect.com/science/article/pii/S0019103514000591` doi: https://doi.org/10.1016/j.icarus.2014.01.028

Quémerais, E., Thiemann, E., Snow, M., Ferron, S., & Schmidt, W. (2019). Multiple Scattering Effects in the Interplanetary Medium: Evaluation Using SOHO SWAN and MAVEN EUVM Lyman α Measurements. *Journal of Geophysical Research: Space Physics*, *124*(6), 3949-3960. doi: https://doi.org/10.1029/2019JA026674

Ramstad, R., Barabash, S., Futaana, Y., Nilsson, H., Wang, X.-D., & Holmström, M. (2015). The Martian atmospheric ion escape rate dependence on solar wind and solar EUV conditions: 1. Seven years of Mars Express observations. *Journal of Geophysical Research: Planets*, *120*(7), 1298-1309. Retrieved from `https://agupubs.onlinelibrary.wiley.com/doi/abs/10.1002/2015JE004816` doi: https://doi.org/10.1002/2015JE004816

Solanki, S. K., Krivova, N. A., & Haigh, J. D. (2013, August). Solar Irradiance Variability and Climate. *Annual Review of Astronomy and Astrophysics*, *51*(1), 311-351. doi: 10.1146/annurev-astro-082812-141007

Sowmya, K., Nèmec, N. E., Shapiro, A. I., Işık, E., Witzke, V., Mints, A., ... Solanki, S. K. (2021, October). Predictions of Astrometric Jitter for Sun-like Stars. II. Dependence on Inclination, Metallicity, and Active-region Nesting. *The Astrophysical Journal*, *919*(2), 94. doi: 10.3847/1538-4357/ac111b

Sowmya, K., Shapiro, A. I., Rouppe van der Voort, L. H. M., Krivova, N. A., &

Solanki, S. K. (2023, October). Modeling Stellar Ca II H and K Emission Variations: Spot Contribution to the S-index. , *956*(1), L10. doi: 10.3847/2041-8213/acf92a

Sowmya, K., Shapiro, A. I., Witzke, V., Nèmec, N. E., Chatzistergos, T., Yeo, K. L., ... Solanki, S. K. (2021, June). Modeling Stellar Ca II H and K Emission Variations. I. Effect of Inclination on the S-index. *The Astrophysical Journal*, *914*(1), 21. doi: 10.3847/1538-4357/abf247

Tagirov, R. V., Shapiro, A. I., Krivova, N. A., Unruh, Y. C., Yeo, K. L., & Solanki, S. K. (2019, November). Readdressing the UV solar variability with SATIRE-S: non-LTE effects. *Astronomy & Astrophysics*, *631*, A178. doi: 10.1051/0004-6361/201935121

Thiemann, E., Chamberlin, P. C., Eparvier, F. G., Templeman, B., Woods, T. N., Bougher, S. W., & Jakosky, B. M. (2017). The MAVEN EUVM model of solar spectral irradiance variability at Mars: Algorithms and results. *Journal of Geophysical Research: Space Physics*, *122*(3), 2748-2767. Retrieved from `https://agupubs.onlinelibrary.wiley.com/doi/abs/10.1002/2016JA023512` doi: https://doi.org/10.1002/2016JA023512

Thiemann, E., Eparvier, F. G., Knoer, V., Al Muharrami, A., & Lillis, R. J. (2021). Solar Extreme Ultraviolet Irradiance Uncertainties for Planetary Studies. *Journal of Geophysical Research: Space Physics*, *126*(1), e2020JA028184. Retrieved from `https://agupubs.onlinelibrary.wiley.com/doi/abs/10.1029/2020JA028184` doi: https://doi.org/10.1029/2020JA028184

Uitenbroek, H. (2001, August). Multilevel Radiative Transfer with Partial Frequency Redistribution. *The Astrophysical Journal*, *557*(1), 389-398. doi: 10.1086/321659

Unruh, Y. C., Solanki, S. K., & Fligge, M. (1999, May). The spectral dependence of facular contrast and solar irradiance variations. *Astronomy & Astrophysics*, *345*, 635-642.

Vaughan, A. H., Preston, G. W., & Wilson, O. C. (1978, June). Flux measurements of Ca II and K emission. *Publications of the Astronomical Society of the Pacific*, *90*, 267-274. doi: 10.1086/130324

Viereck, R., Puga, L., McMullin, D., Judge, D., Weber, M., & Tobiska, W. K. (2001). The Mg II index: A proxy for solar EUV. *Geophysical Research Letters*, *28*(7), 1343-1346. Retrieved from `https://agupubs.onlinelibrary.wiley.com/doi/abs/10.1029/2000GL012551` doi: https://doi.org/10.1029/2000GL012551

Wilson, O. C. (1978, December). Chromospheric variations in main-sequence stars. , *226*, 379-396. doi: 10.1086/156618